Talanta 282 (2025) 126954

Contents lists available at ScienceDirect

Talanta

journal homepage: www.elsevier.com/locate/talanta

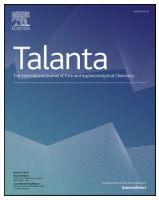

Spatial lipidomic profiles of atherosclerotic plaques: A mass spectrometry imaging study

Sphamandla Ntshangase [a], Shazia Khan [a], Louise Bezuidenhout [a], Taťána Gazárková [a,1], Jakub Kaczynski [a], Stephanie Sellers [b], Nicholas JW. Rattray [c], David E. Newby [a], Patrick WF. Hadoke [a], Ruth Andrew [a,*]

[a] University/BHF Centre for Cardiovascular Science, University of Edinburgh, Edinburgh, EH16 4TJ, UK
[b] Centre for Heart Lung Innovation, St Paul's Hospital and University of British Columbia, Vancouver, Canada
[c] Strathclyde Institute of Pharmacy and Biomedical Sciences, University of Strathclyde, Glasgow, G4 0RE, UK

ARTICLE INFO

Handling editor: Qun Fang

Keywords:
Mass spectrometry imaging
Atherosclerosis
Spatial lipidomics
Histology
Cardiovascular lipid biomarkers

ABSTRACT

Lipids contribute to atherosclerotic cardiovascular disease but their roles are not fully understood. Spatial lipid composition of atherosclerotic plaques was compared between species focusing on aortic plaques from New Zealand White rabbits and carotid plaques from humans (n = 3), using matrix-assisted laser desorption/ionization mass spectrometry imaging. Histologically discriminant lipids within plaque features (neointima and media in rabbits, and lipid-necrotic core and fibrous cap/tissue in humans) included sphingomyelins, phosphatidylcholines, and cholesteryl esters. There were 67 differential lipids between rabbit plaque features and 199 differential lipids in human, each with variable importance in projection score $\geq$1.0 and $p < 0.05$. The lipid profile of plaques in the rabbit model closely mimicked that of human plaques and two key pathways (impact value $\geq$ 0.1), sphingolipid and glycerophospholipid metabolism, were disrupted by atherosclerosis in both species. Thus, mass spectrometry imaging of spatial biomarkers offers valuable insights into atherosclerosis.

1. Introduction

Atherosclerotic cardiovascular disease is a major cause of global mortality, accounting for 50% of deaths in Westernized society despite considerable advances in prevention and treatment [1]. Atherosclerosis is an inflammatory condition characterized by development of lipid-containing plaques in artery walls. The disease advances by lipid accumulation, chronic inflammation, smooth muscle cell proliferation, and extracellular matrix deposition. This, combined with cell death, results in development and expansion of lipid-rich necrotic cores. Advanced lesions are prone to surface erosion or rupture [2], leading to embolization or vessel occlusion, which can trigger lethal cardiovascular events such as myocardial infarction and stroke. Elucidating precise molecular mechanisms driving atherosclerosis is essential to advance treatments, diagnostics and prevention.

Lipids play key roles in atherosclerotic plaque development, initiating formation of fatty streaks, and forming a major component of the necrotic core. Plasma lipidomic signatures have been linked to likelihood of plaque rupture [3,4], but little is known about the risk profile related to the composition of plaques. Therefore, accurate identification of lipid deposits in plaque features is key to understanding disease progression and predicting signatures of plaque vulnerability. Key lipids accumulating in plaques encompass cholesterol and its derivatives (e.g. cholesteryl esters), triglycerides, and phospholipids [5]. Technologies to map individual lipid species within plaque regions are required to unravel the complex composition of these lesions.

Matrix-assisted laser desorption/ionization mass spectrometry (MALDI-MS) imaging is a powerful label-free imaging modality capable of spatially characterizing biomolecules including lipids. With its ability to analyze multiple molecules simultaneously, MALDI-MS imaging is extensively employed to identify new disease biomarkers [6]. For atherosclerotic plaques, MALDI-MS imaging can be combined with histological stains to colocalize molecular patterns of plaque features [7–9].

* Corresponding author. University/BHF Centre for Cardiovascular Science Queen's Medical Research Institute, University of Edinburgh, Edinburgh, EH16 4TJ, UK.
E-mail address: ruth.andrew@ed.ac.uk (R. Andrew).
[1] Department of Analytical Chemistry, Faculty of Pharmacy in Hradec Králové, Charles University, Heyrovského 1203, 500 05 Hradec Králové, Czech Republic

https://doi.org/10.1016/j.talanta.2024.126954
Received 29 May 2024; Received in revised form 18 September 2024; Accepted 24 September 2024
Available online 28 September 2024

Investigating atherosclerosis (a chronic condition that develops silently over several decades) is challenging in humans. Consequently, pre-clinical animal models have proven essential tools for investigations into the pathogenesis and treatment of atherosclerosis. Whilst no animal model completely replicates the condition in humans, rabbits have been used extensively because they exhibit aspects of lipoprotein metabolism consistent with humans, and they develop hypercholesterolemia and lesions (initially fatty streaks) when exposed to a high cholesterol diet [10]. Furthermore, accelerated development of fibroproliferative lesions can be induced in rabbits by combining dietary modification with intraluminal injury [11]. Although the use of rabbit models has declined with the advent of mice with genetic modifications in apolipoprotein E (apoE) and low-density lipoprotein (LDL) receptors [12], rabbits remain valuable for studying the etiology of atherosclerosis. Indeed, mice do not readily develop atherosclerosis without genetic manipulation. Furthermore, the lesion-bearing arteries isolated from the rabbits used in this study were similar in size to the specimens isolated from patients (lesion bearing arteries from murine models of atherosclerosis would likely have been at, or beyond, the limit of detection for this technique). Previous studies have not fully curated and compared the spatial lipid composition of plaques in rabbits and humans. Utilizing MALDI-MS imaging, this study tests the hypothesis that plaques in a rabbit model of atherosclerosis will exhibit lipid profiles comparable to those in humans.

2. Experimental section

Chemicals and Reagents: Acetonitrile, ethanol, and water (LC-MS grade, Fisher Scientific, Loughborough, UK); red phosphorous and gelatin (porcine skin), polyvinylpyrrolidone (PVP), hydroxypropyl methylcellulose (HPMC), trifluoroacetic acid (TFA), 1,5-diaminonaphthalene (DAN) and α-cyano-4-hydroxycinnamic acid (CHCA) (Sigma-Aldrich Gillingham, UK); monoclonal α-smooth muscle actin (1A4 clone, GA611, RRID: AB_262054) and antihuman CD68 (L26 clone, M0756, RRID: AB_2074844) antibodies (Dako Agilent Pathology Solutions, Cheshire, UK).

Biological Samples: Three male New Zealand White rabbits (Charles River Laboratories, Elphinstone, UK) were housed for >1 week prior to being fed a high cholesterol diet (C30262 Purina 5322 Rabbit chow with 0.2% cholesterol; Research Diets Inc., New Brunswick, USA). The New Zealand White rabbit strain has a well-characterized genetic background and has been used extensively for investigation of arterial remodeling in atherosclerosis. The New Zealand White rabbit is notably susceptible to diet-induced atherosclerosis (and development of lesions can be accelerated by combination with intra-luminal injury), making it the model of choice for the pharmaceutical industry and preclinical studies of atherosclerosis. It has been used both for investigations into the pathogenesis of atherosclerosis and for pre-clinical testing of potential new therapies [10,13]. Procedures were performed in accordance with ARRIVE guidelines, under the provisions of the Animals Scientific Procedures Act (1986) and approved by the local Ethics Committee (60/3867). Animals underwent repeated balloon injury to the abdominal aorta (1 and 3 months after start of diet), and were allowed to recover for 6 months to induce atherosclerosis-like neointimal lesions [11]. Rabbits were then killed by overdose of sodium pentobarbitone (i.v. Euthatal, *via* marginal ear vein) and lesion-bearing sections of aortae harvested onto dry ice and stored at −80 °C.

Carotid plaques were collected from three male patients (72–80 years; NHS Lothian) who presented with symptoms such as stroke or transient ischemic attack and underwent endarterectomy (Royal Infirmary of Edinburgh, East of Scotland Research Ethics Service REC 1 (15/ES/0094). The patients' total cholesterol concentrations ranged from 3.3 to 4.1 mmol/L, and their triglyceride levels from 0.6 to 1.7 mmol/L. Two patients had a history of smoking, and one patient was on statin therapy. Carotid plaques were snap-frozen in liquid nitrogen immediately after carotid endarterectomy and stored at −80 °C.

Tissue Handling and Preparation for MS Imaging: Rabbit aortae were attached to the chuck using gelatin (10% w/v), while human carotid plaques were embedded in 7.5% HPMC and 2.5% PVP [14]. Serial tissue cryosections (10 μm) were cut using a CryoStar NX50 cryostat (Fisher Scientific) at −16 °C with MX35 Premier Blades (Fisher Scientific) and thaw-mounted onto either SuperFrost Plus (Fisher Scientific) or indium-tin oxide (ITO)-coated glass slides (Bruker Daltonics, Bremen, Germany). The sections were vacuum-sealed and stored at −80 °C. Prior to imaging, slides were desiccated for 30 mins at room temperature (20–22 °C) and coated with CHCA (10 mg/mL in 70/29.9/0.1 acetonitrile/water/TFA) or 1,5-DAN (5 mg/mL in 90/10 acetonitrile/water) using an HTX M3 sprayer (Table S1). Spray parameters for CHCA/DAN were: temperature, 75/77 °C; flow rate, 0.24/0.12 mL/min; nozzle velocity, 1200 mm/min (both); track spacing, 1.0/3.0 mm; nitrogen pressure, 10 psi (both); drying time, 5 s (both); number of passes, 2/12; matrix density, 4/2 μg/mm^2. Slides were scanned using an Epson Perfection V370 optical scanner (London, UK).

MALDI Q-ToF MS Imaging: Data acquisition was performed using High-Definition Imaging v1.5 and MassLynx v4.2 (Waters Corporation, Wilmslow, UK) software in MALDI$^+$ and MALDI$^-$ modes on a MALDI quadrupole time-of-flight (Q-ToF) mass spectrometer (Synapt G2Si MS, Waters) equipped with a 355 nm Nd:YAG laser rastered at a frequency of 1 kHz and spatial resolution of 75 × 75 μm^2. Before data acquisition, external calibration was carried out with red phosphorous signals in both modes. Final MS imaging was performed in sensitivity mode, with trap and transfer collision energies of 4 and 2 V respectively, resulting in mass resolution of ~17 000 full-width at half-maximum (FWHM) at m/z 400 in the range m/z 100–1200.

MALDI FT-ICR MS Imaging: High-mass-resolution data were acquired from sections on ITO-coated slides using a 12T SolariX Fourier transform ion cyclotron resonance mass spectrometer (FT-ICR MS), operated by ftmsControl v.2.2 (Bruker Daltonics) and equipped with a Smartbeam II 2 kHz frequency Nd:YAG laser (355 nm). A time domain file size of 1 M was used to acquire positive and negative ion mode data by firing 300 laser shots/pixel (power 42%, mass resolution of ~400 000 at FWHM at m/z 400).

Histology and Immunohistochemistry: After MS imaging, tissue sections were washed with ethanol to remove matrix and stained with hematoxylin and eosin (H&E). Adjacent sections (5 μm) were stained by oil red O (neutral lipids) [15], alizarin red S (calcium deposits), or underwent immunohistochemical analysis (Supplementary information) for smooth muscle cells (alpha-smooth muscle actin) or macrophages (CD68). High-resolution optical images of stained tissues (ZEISS Axioscan 7×Microscope Slide Scanner, 20× magnification) were overlaid with MS images.

Data Processing: Raw data were imported into LipostarMSI (Molecular Horizon Srl, Perugia, Italy) [16]. Peak detection was performed with signal-to-noise ratio thresholds of 5. Average spectra were Lock-Mass corrected using sphingomyelin, SM 34:1 as $[M+Na]^+$ or $[M\text{-}CH_3]^-$. Peaks were filtered with a tolerance of 0.05 for Synapt and 0.0025 Da for FT-ICR, respectively. Images were subject to hotspot removal at 99.98%. Unsupervised clustering methods including the bisecting K-means algorithm revealed regions defined by spatial segmentation. Training Regions of Interest (ROIs) were defined following histological annotations to compare media and neointima (rabbit) and necrotic core, and fibrous cap (human). We defined 6 ROIs within each lesion area to capture intra-lesional heterogeneity (Fig. S1). The size of each ROI was standardized to ensure comparable data points across samples. Each ROI comprised 4 (rabbit aorta) or 9 (human carotid plaque) ablation pixels. ROI data were normalized against total ion current (TIC) and data matrices exported.

Lipid Identification: Lipids were identified by searching FT-ICR MS data against the LIPID MAPS database (LipostarMSI) with a threshold of <2 Δppm [17]. m/z values (Synapt G2Si MS) were compared to those in the FT-ICR MS dataset. Potential isobaric lipids linked to m/z values were evaluated. MALDI MS/MS fragmentation (Synapt G2Si MS) was

performed on plaque sections, guided by spatial features. Fragmentation of individual ions was optimized by customized adjustments of collision energy (20–40 V). A uniform low mass (LM) resolution was set at 15 and used across all MS/MS experiments to ensure consistency. Final identities were manually inspected, considering isotopic patterns. Potential misidentifications were excluded.

Statistical Analyses: Data matrices underwent pre-processing, including median normalization and Pareto scaling, prior to multivariate analysis (Figs. S2–S3) (MetaboAnalyst 6.0 www.metaboanalyst.ca). Heatmaps were generated on open-source R v4.1.3/R Studio software v4.2.2 using R package, pheatmap v1.0.12, to identify patterns of lipids among ROIs following 'Euclidean distance' function. Orthogonal partial least squares for discriminant analysis (OPLS-DA) highlighted differences between plaque features, including neointima and media (rabbit) and the fibrous cap and necrotic core (human).The measure of the model's quality was R^2Y, while its predictability was represented by Q^2 (0.5 threshold for both) [18]. Identification of significantly different lipids was based on variable importance in the projection (VIP) scores derived from the OPLS-DA model and p-values from Student's *t*-test, corrected for multiple comparisons (Benjamini-Hochberg-based false discovery rate (FDR)). Lipids meeting criteria of VIP score $\geq$1.0 [19] and $p < 0.05$ were considered statistically different. Lipid pathways were analyzed by MetaboAnalyst 6.0 and Kyoto Encyclopedia of Genes and Genomes (KEGG).

3. Results and discussion

Method Optimization: Sectioning efficiency of highly calcified human plaques was improved by embedding plaques in 7.5% HPMC and 2.5% PVP [14] (Fig. S4). Structural support reduced tissue distortion and damage and maintained spatial precision with negligible ion suppression. CHCA (70/29.9/0.1 acetonitrile/water/TFA) and DAN (90/10 acetonitrile/water) were deemed most suitable matrices and offered substantial lipid coverage. Previous studies of lipid detection in atherosclerotic plaques have predominantly employed 2,5-dihydroxybenzoic acid, applied through sublimation [8,9], instead of a wet spray technique.

Histopathological Observations (Rabbit): Distinct features including neointima and media, were evident in the rabbit atherosclerotic aorta (Figs. S1, S5). Oil Red O staining revealed that most neutral lipids accumulated in the neointima (Fig. S5A), while alizarin red staining showed lack of calcification in rabbit plaques (Fig. S5B).

Lipid Annotation (Rabbit): Key lipid classes were identified (Fig. 1), including diacylglycerols (DG), lysophosphatidylcholines (LPC), phosphatidylcholines (PC), sphingomyelin (SM), lysophosphatidic acids (LPA), phosphatidic acids (PA), lysophosphatidylethanolamines (LPE),

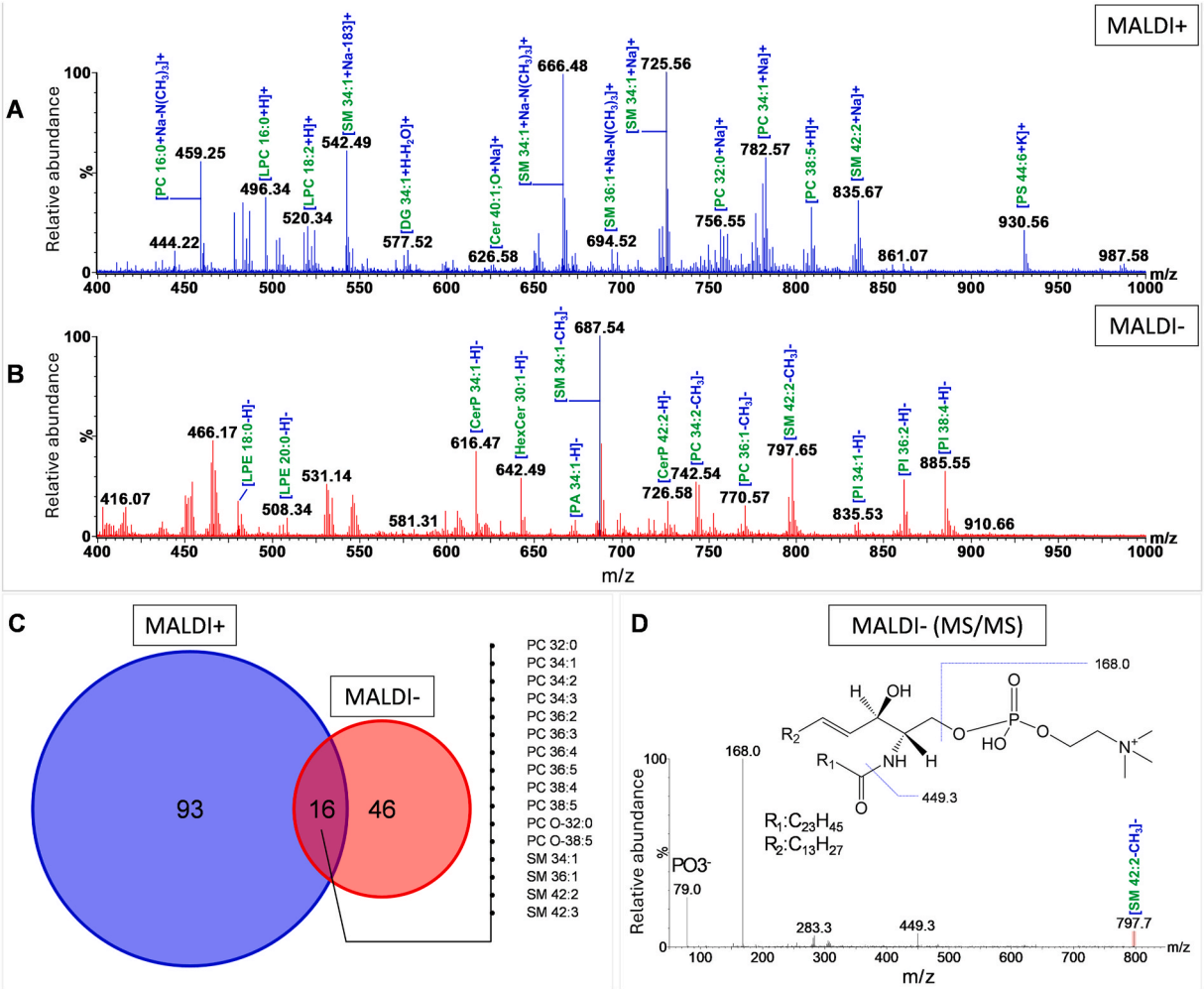

Fig. 1. Mass spectra from atherosclerotic rabbit aorta's neointima, acquired using a SYNAPT G2-Si HD MS in **A**) $MALDI^+$ mode and **B**) $MALDI^-$ mode. **C**) Venn diagram: Lipids detected in $MALDI^+$ and $MALDI^-$ modes, with overlap shown. **D**) MALDI-MS/MS spectrum shows fragmentation of a sphingomyelin $[SM\ 42:1\text{-}CH_3]^-$ at *m/z* 797.65. Cer: ceramide, HexCer: monohexosylceramide, CerP: ceramide-1-phosphates, DG: diacylglycerol, LPC: lysophosphatidylcholine, SM: sphingomyelin, PC: phosphatidylcholine, PC-O: 1-alkyl,2-acylglycerophosphocholines, PS: phosphatidylserine, LPE: lysophosphatidylethanolamine, PI: phosphatidylinositol, PA: phosphatidic acids.

cholesterol esters (CE), phosphatidylglycerols (PG), phosphatidylinositols (PI), and phosphatidylserines (PS), amongst others. High abundances of SM and PC species were seen in both MALDI$^+$ (Fig. 1A) and MALDI$^-$ modes (Fig. 1B). The most abundant ion in both modes was *m/z* 725.5568, identified as [SM 34:1+Na]$^+$, (Δ0.78 ppm). Following putative identification, MS/MS was pivotal in identification (Figs. S6–S7). 155 lipids were identified in rabbit aortic plaques, with 109 detected in MALDI$^+$ and 62 in MALDI$^-$ modes (Fig. 1C). 16 lipids were detected in both modes, comprising SM and PC species identified as both [M+Na]$^+$ and [M-CH_3]$^-$ ions. An example of fragmentation of [SM 42:1-CH_3] is shown (Fig. 1D) with further examples in Figs. S6–S7.

In MALDI$^+$, post-source decay artifacts from phosphocholine headgroup, mainly from SM, LPC and PC species were identified, generated through loss of trimethylamine ([M+Na-59]$^+$) (Fig. 1A), phosphocholine ([M+Na-183]$^+$ and [M+Na-205]$^+$) [20]. These artifacts can be easily misidentified since they are isobaric to LPA and PA sodiated ions, in the cases of LPC and PC, respectively. Multiple adducts of the same lipid were also observed ([M+Na]$^+$, [M+H]$^+$, [M+K]$^+$). Only the most abundant lipid adducts (mainly [M+Na]$^+$) were considered.

Differential lipids (Rabbit): ROIs were combined and lipids not consistently present across replicates excluded. The unified data matrix, (three biological replicates), underwent multivariate classification, and

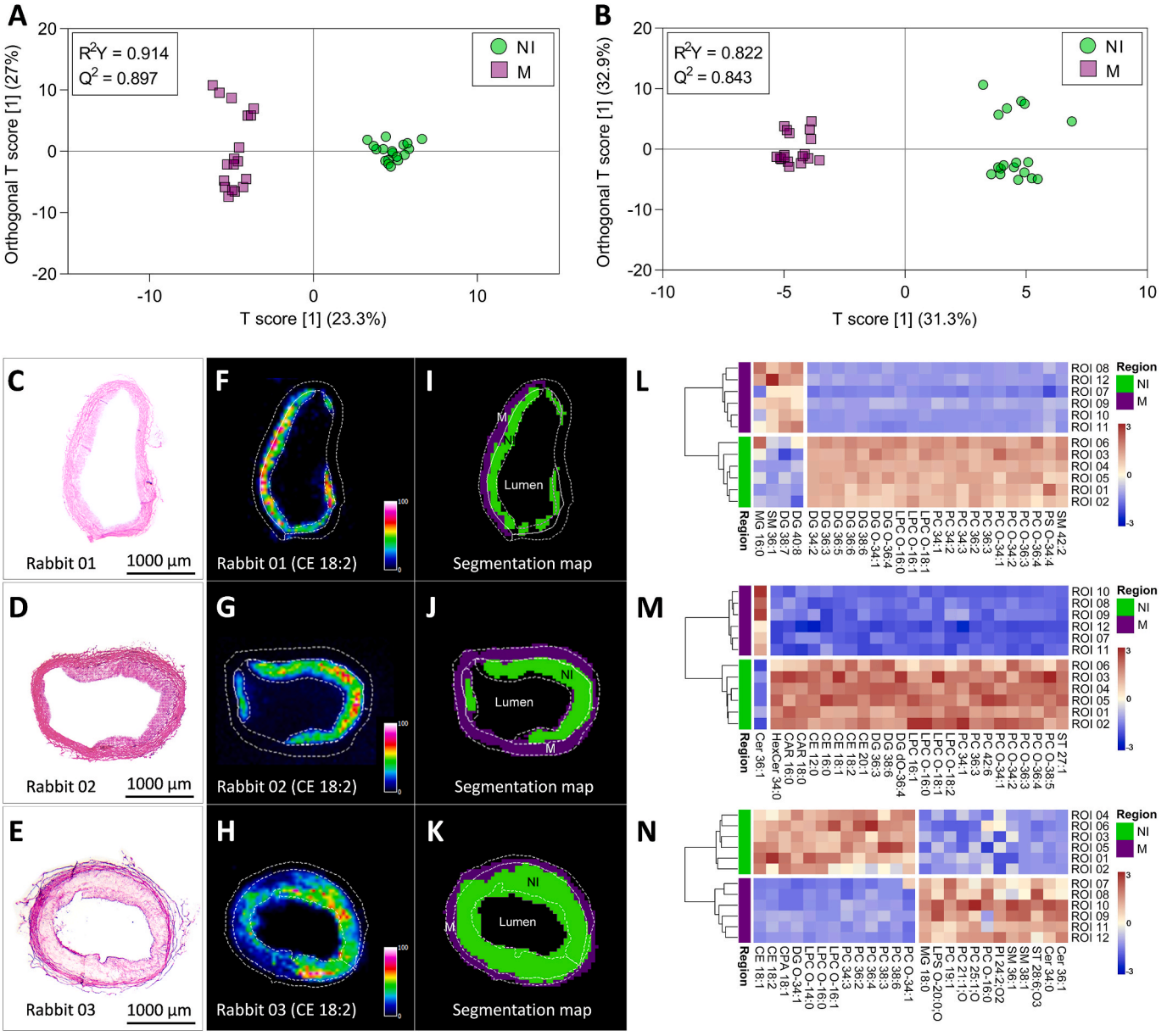

Fig. 2. Orthogonal partial least squares for discriminant analysis scores plot demonstrating distinct separation of regions of interest (ROIs) (n = 6 ROIs/aortic feature) in the neointima (NI) and media (M) of rabbit aortic plaques based on data acquired in (**A**) MALDI$^+$ and (**B**) MALDI$^-$. R^2Y and Q^2 values represent goodness of fit and predictability, respectively. **C–E**) H&E-stained images of rabbit aortic tissue sections. **F–H**) MALDI-MS imaging of an exemplar lipid, cholesterol ester [CE 18:2], enriched in the neointima (NI) (Scale bar, 1000 µm). Six cloned square regions of interest comprising 4 ablation pixels were profiled in aortic features (neointima, media). **I–K**) Unsupervised bisecting k-means segmentation of lipids following MALDI$^+$ MS imaging of three rabbit atherosclerotic aortas. **L–N**) Unsupervised hierarchically clustered heatmaps of the top 25 differential lipids with variable importance in projection score ≥1.0. CAR: acyl carnitine, CE: cholesterol ester, Cer: ceramide, CPA: monoacyl cyclic glycerophosphatidic acid, DG: diacylglycerol, DG dO: dialkylglycerols, DG-O: 1-alkyl, 2-acylglycerols, HexCer: monohexosylceramide, LPC: lysophosphatidylcholine, LPC-O: monoalkylglycerophosphocholines, LPS-O: monoalkylglycerophosphoserines, MG: monoacylglycerols, PC: phosphatidylcholine, PC-O: 1-alkyl, 2-acylglycerophosphocholines, PI: phosphatidylinositol, PS-O: 1-alkyl,2-acylglycerophosphoserines, SM: sphingomyelin, ST: sterol.

feature analysis. OPLS-DA modelling showed distinct separation between the media and neointima (Fig. 2A and B), with $R_2Y = 0.914$ and $Q^2 = 0.897$ ($MALDI^+$) and $R_2Y = 0.822$ and $Q^2 = 0.843$ ($MALDI^-$) [18]. In $MALDI^+$ mode, 45 differential lipids were distinguished, with 30 in the neointima and 15 in the media. In $MALDI^-$ 28 differential lipids were identified, with 16 in the neointima and 12 in the media. In $MALDI^+$ mode, PC 36:2 and SM 36:1 showed the highest VIP scores $\geq$1.0 (Table S2), distinguishing neointima and media, respectively. In contrast, in $MALDI^-$, PA 36:3 and PS 38:4 served as notable discriminators between neointima and media, respectively (Table S2).

Fig. 2 shows H&E (Fig. 2C–E), MS (Fig. 2F–H), segmentation (Fig. 2I–K) images and heatmaps of the top 25 differential lipids (Fig. 2L–N) highlighting that most lipids were exclusive to the neointima. However, a subset was exclusive to the media. Many lipids were distributed throughout the tissue. Triacylglycerols (TG) exclusively localized in the perivascular adipose tissue surrounding the aorta, and were excluded in the final analysis (Fig. S8).

Pathway Perturbations in Atherosclerosis (Rabbit): Three differential lipid pathways (impact values > 0.10) [21] were revealed in $MALDI^+$ mode (Fig. 3A, Table S3), comprising glycerophospholipid, ether lipid, and sphingolipid metabolism. Three were also identified in $MALDI^-$ (Fig. 3B); glycerophospholipid, ether lipid, and glycerolipid metabolism aligning with previous studies on atherosclerosis [22].

Glycerophospholipid metabolism in rabbit atherosclerosis (Fig. 3C) involved key constituents including DG, PC, PE, PS, monoacylglycerophosphoserines (LPS), LPE, LPA and PA. Most abundant lipid ions in both $MALDI^+$ (Fig. 1A) and $MALDI^-$ (Fig. 1B) were sodiated PC and SM species. Glycerophospholipids play crucial roles in cellular processes including signal transduction and inflammation, central to atherosclerotic processes [23]. Perturbations in glycerophospholipid metabolism suggest disruption in cell membrane integrity, lipid homeostasis and inflammation, pivotal factors in plaque formation and progression.

Mapping of glycerolipid metabolism highlighted LPA and PA for further consideration. With well-established pro-inflammatory and pro-atherogenic effects, LPA contributes to endothelial dysfunction, monocyte adhesion, and smooth muscle cell migration, key elements in plaque formation [24]. An imbalance in PA levels, a crucial phospholipid biosynthesis intermediate, can modify membrane composition by altering phospholipid ratios. This could initiate cellular responses such as signal transduction or morphological changes in arterial walls.

Distinctive perturbations in ether lipid metabolism linked predominantly to monoalkylglycerophosphocholines (LPC-O), 1-alkyl,2-acylglycerols (DG-O), 1-alkyl,2-acylglycerophosphocholines (PC-O), and 1Z-alkenylglycerophosphoethanolamines (LPE-O). Ether lipids are a class of peroxisome-derived glycerophospholipids and glycerolipids. Platelet activating factor (PAF) for example belongs to the group of 1-*O*-alkyl-2-acetyl-*sn*-glycero-3-phosphocholines produced by endothelial cells and macrophages and plays a key pro-inflammatory role in atherosclerotic plaque formation [25]. PAF comprises a set of 1-*O*-alkyl-2-acetyl-*sn*--glycero-3-phosphocholines (PC-O) with differing hydrocarbon lengths at *sn*-1 and a consistent acetyl group at *sn*-2 (e.g., PC O-34:1).

Key components of sphingolipid metabolism implicated include SM and Cer which were elevated in the neointima relative to the media. Pro-atherogenic sphingolipids influence initiation and progression of atherosclerosis [26], modifying signal transduction, differentiation, proliferation, and apoptosis [27,28]. In plaques, enzymatic hydrolysis of SM to Cer by acid sphingomyelinase initiates aggregation and fusion of lipoproteins including low-density lipoprotein [29,30]. Cer underpins cellular processes such as apoptosis, necrosis, and autophagy-dependent cell death [31].

Histopathological Observations Human Carotid Plaques: Human plaques showed distinct regions including necrotic core, fibrous cap and other fibrous tissue but were more variable in structure than the rabbit. A necrotic core was observed in the plaque from Patient 01 (Fig. 4D), but a clearly defined fibrous cap was lacking. Instead, distinct regions of acellular fibrous areas (including calcium deposits) were observed. The plaque from Patient 02 (Fig. 4E) was advanced and fibrocalcific [32,33], featuring extensive sheet calcification within the underlying intimal layer, supported by fibrous tissue and a relatively thin but discernible fibrous cap, rich in vascular smooth muscle cells (Fig. S9). Notably, a necrotic core was absent. The advanced plaque of Patient 03 (Fig. 4F), featured a large necrotic core shielded by fibrous cap. Thick fibrous caps associate with more stable plaques, less likely to lead to acute cardiovascular events [34]. Conversely, fibrous caps can be a site of inflammation, and a thin cap makes it more vulnerable to rupture [35]. Therefore, lipids present in the cap may influence stability. Necrotic cores are a sign of advanced disease linked with plaque instability.

Lipid Identification in Human Carotid Plaque: Given the pronounced variability, each specimen underwent individual analysis. 383 lipids were identified in human carotid plaques across all three patients, with 120 in $MALDI^+$ and 297 in $MALDI^-$ and 34 lipids in both ion modes (Fig. S10). Lipids identified encompassed diverse classes, the most abundant being SM, PC, DG, Cer and LPC. PC 34:2 and SM 34:1 were consistently highly abundant. Distinct distributions were found for PC (fibrous cap) and SM (necrotic core). In the $MALDI^+$ ion mode data, 43, 43, and 58 lipids discriminated the necrotic core/neointimal fibrous tissue from the fibrous cap for Patients 01, 02, and 03, respectively. Similarly, differential lipids in $MALDI^-$ mode were 72, 49, and 87 for Patients 01, 02, and 03, respectively.

Exemplar MS images of human carotid plaques (Fig. 4G–I) show LPC16:0 detected as $[M+Na]^+$, one of the most abundant ions, along with segmentation maps (Fig. 4J–L) defining important features. Heatmaps (Fig. 4M−O) show the top 25 significantly different lipids across distinct plaque features. Notably, the necrotic core exhibits high abundance of lipids such as LPC, CE, SM, Cer, PS, and TG. These localization patterns are consistent with those observed in previous spatial lipidomic studies [8,9] and are indicative of processes associated with cell death, inflammation, and lipid accumulation. Conversely, the fibrous cap is characterized by elevated levels of PC and DG, which are essential components in cellular signaling and structural stability. These nuanced spatial variations in lipid composition provide critical insights into the underlying molecular processes driving plaque heterogeneity. The OPLS-DA model was satisfactory in discriminating plaque features

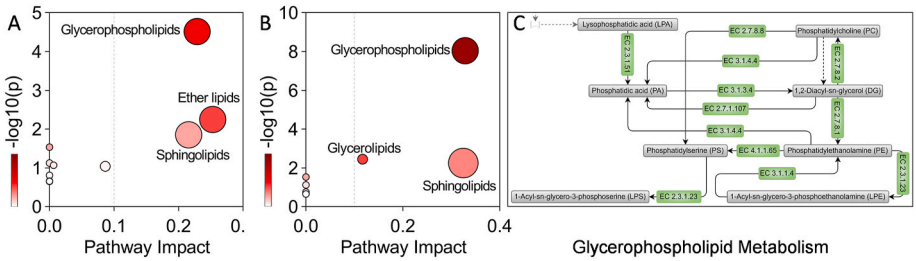

Fig. 3. Contributing pathways in rabbit atherosclerosis (aortae) from **A)** $MALDI^+$ and **B)** $MALDI^-$ data (MetaboAnalyst 6.0). Node size represents impact values of pathways and colour gradation (white to red) significance (p-value), with most reliable pathways in the upper right. **C)** Glycerophospholipid metabolism - *Oryctolagus cuniculus* (rabbit) pathway map from KEGG showing key lipid classes from data acquired in both modes. Green boxes represent enzyme catalysed reactions.

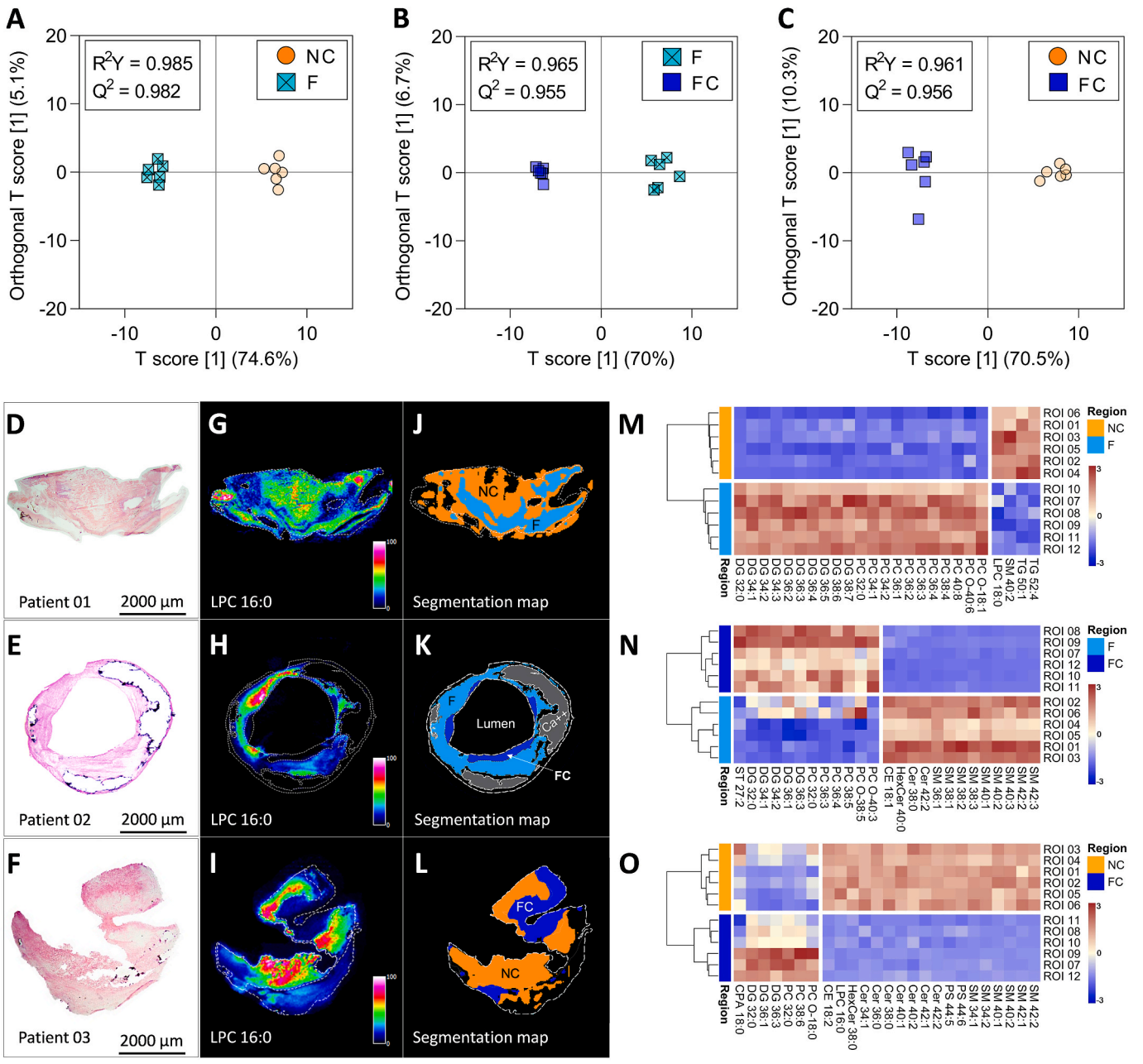

Fig. 4. MALDI$^+$: Orthogonal partial least squares for discriminant analysis scores plots comparing plaque features in **A**) Patient 01, **B**) 02 and **C**) 03. R^2Y = goodness of fit; Q^2 = predictability. F: fibrous tissue, FC: fibrous cap, NC: necrotic core. **D-F**) H&E-stained images of human carotid plaque sections. **G-I**) MALDI-MS imaging showing enrichment of an exemplar lipid, lysophosphatidylcholine (16:0) [LPC 16:0] in the other fibrous tissue (F) and necrotic core (NC), with lower abundance in the fibrous cap (FC), (n = 3) (Scale bar, 2000 µm). **J-L**) Unsupervised bisecting k-means segmentation map of lipids. **M-O**) Corresponding heatmap of top 25 feature-specific lipids differentiating the F, NC, and FC. CE: cholesterol ester, Cer: ceramide, CPA: monoacyl cyclic glycerophosphatidic acid, DG: diacylglycerol, HexCer: monohexosylceramide, LPC: lysophosphatidylcholine, PC: phosphatidylcholine, PC-O: 1-alkyl,2-acylglycerophosphocholines, PS: phosphatidylserines, SM: sphingomyelin, ST: sterol, TG: triacylglycerol.

(Table S4), in both MALDI$^+$ (Fig. 4A–C) and MALDI$^-$ (Fig. S11) modes. Similar to rabbit, glycerophospholipid metabolism was the most significantly affected pathway in all patients, followed by sphingolipid metabolism.

Pathway Perturbations in Atherosclerosis (Human): The results from both MALDI$^+$ and MALDI$^-$ modes (Table 1, Tables S5–S7) highlighted four crucial lipid pathways including metabolism of glycerophospholipids, glycerolipid, ether lipids and sphingolipids. Representative lipidome maps derived from the plaque 03 illustrate perturbed lipid pathways in both MALDI$^+$ (Fig. 5A, Table S4) and MALDI$^-$ (Fig. 5B–Table S4) analyses (Figs. S12–S13).

Sphingolipid metabolism (Fig. 5C) in human carotid plaques predominantly involved SM, Cer, CerP, glucosylceramide (GluCer), galactosylceramide (GalCer) and lactosylceramide (LacCer), mainly localised in the necrotic core. SM constitute a significant portion of the phospholipids in the necrotic core, a finding that has been confirmed by several studies to date [8,9,35,36]. Some studies have further associated SM with plaque instability and inflammation [8,9]. As in previous studies, GluCer and LacCer accumulated within plaques [37], other sphingolipids including GluCer is a precursor of various glycosphingolipids, including Cer, important for cell membrane structure and signaling. GluCer are hydrolyzed by glucosylceramidase (EC:3.2.1.45)

Table 1
Most impactful metabolic pathways in human carotid artery atherosclerotic plaques following MALDI analyses.

MALDI$^+$			
Lipid pathway	Pathway impact value and p-value		
	Patient 01	Patient 02	Patient 03
Glycerophospholipid metabolism	0.12 and 5.68 × 10^{-4}	0.16 and 4.39 × 10^{-5}	0.16 and 6.78 × 10^{-5}
Glycerolipid metabolism	0.10 and 2.61 × 10^{-3}	[a]	0.30 and 5.05 × 10^{-3}
Ether lipid metabolism	[a]	0.11 and 6.49 × 10^{-3}	[a]
Sphingolipid metabolism	[a]	0.22 and 1.63E^{-02}	0.43 and 4.20 × 10^{-5}
MALDI$^-$			
Glycerophospholipid metabolism	0.37 and 5.43 × 10^{-9}	0.33 and 3.95 × 10^{-8}	0.37 and 6.90 × 10^{-10}
Sphingolipid metabolism	0.35 and 1.22 × 10^{-4}	0.07 and 1.13 × 10^{-3}	0.35 and 2.78 × 10^{-4}
Ether lipid metabolism	0.24 and 5.84 × 10^{-4}	0.12 and 7.87 × 10^{-3}	0.41 and 4.06 × 10^{-5}
Glycerolipid metabolism	0.12 and 8.20 × 10^{-3}	[a]	0.12 and 5.37 × 10^{-4}

[a] Pathway impact value < 0.10.

to free Cer and glucose. Perturbed levels of either Cer or GluCer contribute to inflammatory responses and induce apoptosis in vascular smooth muscle cells [38–40]. Imbalance may directly influence progression of atherosclerotic plaques [41].

The glycerophospholipid pathway in human carotid plaques involved diverse lipids, including DG, PC, LPC, PS, LPE, LPA, PA, monoacylglycerophosphoinositols (LPI) and PI. PA is a crucial intermediate in the synthesis of various membrane glycerophospholipids, including PC. In human carotid plaque, PCs were primarily localized in the fibrous cap and along the luminal lining but the implications of this pattern, including whether it has beneficial or detrimental effects, are not yet fully understood. Plaque stability is associated with characteristics such as a substantial fibrous cap and increased VSMCs density [34] but, specific roles of PCs in these processes require further research.

The key mediators of glycerolipid metabolism (Fig. 5) included DG, monoacylglycerol (MG), LPA, PA, monoacylglycerophosphoinositols (LPI), and PI. DG and MG are crucial intermediates in triglyceride and phospholipid synthesis [42]. LPI and PI are essential glycerophosphoinositols involved in signal transduction and membrane dynamics [43].

Ether lipids in human carotid plaque included 1-alkyl,2-acylglycerophosphates (PA-O), PC-O, LPE-O, and 1-alkyl,2-acylglycerophosphoethanolamines (PE-O), and are all implicated in pro-inflammatory responses, lipid homeostasis and cellular activities associated with inflammation [25].

Rabbit vs Human Atherosclerosis: Animal models are crucial in advancing understanding of molecular mechanisms underlying atherosclerosis [44,45]. Rabbits develop severe hypercholesterolemia and atherosclerotic lesions when fed a cholesterol-rich diet [46]. This combined with repeated balloon angioplasty of rabbit abdominal aortae produces large complex, plaques, structurally similar to the fibrous plaques associated with developing disease in humans [47]. Again, similar to humans, HDL is the predominant plasma lipoprotein in rabbits [46] (in contrast to rats and mice, where plasma cholesterol is carried in LDL and VLDL) [46]. Furthermore, the relatively large lesions in rabbits can be identified and analyzed *ex vivo* using MS imaging [48] and other clinical tools, e.g. positron emission tomography-magnetic resonance imaging (PET-MRI) [11,49,50]. Here rabbit atherosclerotic lesions demonstrated relatively consistent structure between animals, providing complete cross-sections of the abdominal aorta exhibiting a clearly-defined fibroproliferative neointima (bordered by the lumen and the internal elastic lamina) within a readily identifiable medial layer. This type of lesion is comparable to the fibrous plaque characteristic of developing atherosclerosis. In contrast presentation of human carotid artery plaques was more variable, including features such as necrotic cores, fibrous caps, and calcifications, more typical of the complicated plaque associated with advanced disease. The relative consistency and simplicity of lesions in the rabbit aorta facilitates interpretation of the lipid data in relation to plaque constituents. Furthermore, the ability to use the rabbit model to generate different stages of lesion development (e.g. fatty streaks to replicate the early stages of lesion development; fibroproliferative lesions to replicate the classic advancing lesion of atherosclerosis) [10] provides an opportunity for use of MS Imaging to provide a systematic understanding of the early stages of atherosclerosis, facilitating the study of disease progression and the evaluation of potential clinical therapeutic interventions.

Rabbits models bridge the gap between cardiometabolic studies in mice and humans, since they share most lipid and lipoprotein metabolism features with humans, including, response to a high cholesterol diet, cholesteryl ester transfer protein (CETP), apolipoprotein B-100 bound to apolipoprotein(a) amongst others [51]. At a lipidomic level there were notable similarities and differences in profiles and localization patterns between species. We found 44 common lipids from 14 lipid classes between the two species (Fig. S14), highlighting potential convergent pathways relevant to atherosclerosis. Amongst the common lipids were the most abundant lipid classes, including CE, Cer, SM, and PC which have been previously linked to cardiovascular diseases, including atherosclerosis [4,52]. By comparing these metabolic changes from the rabbit model to human plaques, we can gain a clearer understanding of the specific lipids that contribute to plaque formation. With

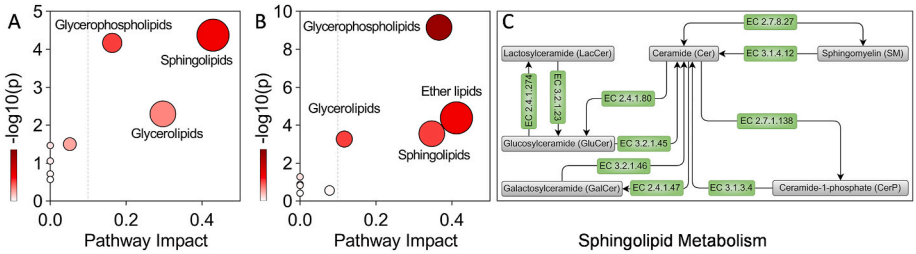

Fig. 5. Contributing pathways in human carotid plaques from **A**) MALDI$^+$ and **B**) MALDI$^-$ data (MetaboAnalyst 6.0). Node size represents impact values of pathways, and colour gradient (white to red) significance (p-value), with most reliable pathways in upper right. **C**) Sphingolipid metabolism - *Homo sapiens* (human) pathway map generated from KEGG showing key lipid classes involved from data acquired in both modes. Green boxes represent enzyme catalysed reactions.

further investigations in larger cohorts, this knowledge will be utilized for diagnostic purposes, identifying vulnerable plaques. Furthermore, the biomarkers annotated may be integrated with clinical imaging modalities, such as PET-MRI, to enhance the targeting of these lipids for improved disease management and treatment.

The predominant localization of PC in the neointima of rabbit lesions contrasts with their prevalence in fibrous caps of human plaques. PCs are major components of cellular membranes and mainly co-localized with smooth muscle cells [53]. Despite variations in plaque features and disease stages, similar perturbations in glycerophospholipid, glycerolipid, ether lipid and sphingolipid metabolic pathways in atherosclerosis were identified in both rabbits and humans, providing valuable insights into shared pathophysiological mechanisms.

Certain limitations must be acknowledged. Induction of chronic hypercholesterolemia through cholesterol-rich feeding in rabbits can lead to inflammation and hepatic toxicity. When considering lesions in rabbits, the ratio of lipid-rich cores to fibrous caps (sometimes completely absent) may not mirror the human condition. Similarly, whereas calcification is common in advanced lesions in humans, it is less frequently observed in rabbit lesions, more akin to pre-calcific stage [54]. However, as non-calcified plaques account for most cardiovascular events [12], lack of calcified lesions does not reduce the translational validity of the rabbit model in diagnostic and therapeutic studies.

The sample size (n = 3, analyzed in technical triplicates) was relatively low albeit stringent data analysis criteria were applied. Moreover, challenges in fully characterizing fibrous caps and necrotic cores of human carotid plaques in a small sample size prevent definitive conclusions regarding plaque vulnerability or stability. Nevertheless, our study successfully identified both distinct and consistent features of rabbit and human plaques, offering valuable comparative insights into multifaceted atherosclerotic cardiovascular disease.

4. Conclusions

Integrating histology with MALDI-MS imaging of individual lipid species in rabbit atherosclerotic aortas and human carotid plaques yielded spatial information of pivotal pathogenic lipids. Rabbit plaques exhibited spatial lipid profiles closely resembling those of humans, reinforcing rabbits as reliable pre-clinical models. Also, comparable metabolic changes across specific plaque features including neointima, media, fibrous cap, and necrotic core, hint at similarities in disease development that may provide potential therapeutic targets.

CRediT authorship contribution statement

Sphamandla Ntshangase: Writing – original draft, Visualization, Methodology, Investigation, Formal analysis, Conceptualization. **Shazia Khan:** Writing – review & editing, Methodology. **Louise Bezuidenhout:** Writing – review & editing, Methodology, Conceptualization. **Taťána Gazárková:** Writing – review & editing, Methodology. **Jakub Kaczynski:** Writing – review & editing, Methodology. **Stephanie Sellers:** Writing – review & editing. **Nicholas JW. Rattray:** Writing – review & editing. **David E. Newby:** Writing – review & editing, Supervision, Resources, Conceptualization. **Patrick WF. Hadoke:** Writing – review & editing, Supervision, Resources, Methodology, Conceptualization. **Ruth Andrew:** Writing – review & editing, Supervision, Resources, Project administration, Funding acquisition, Conceptualization.

Declaration of competing interest

The authors declare that they have no known competing financial interests or personal relationships that could have appeared to influence the work reported in this paper.

Data availability

I have shared a link to my data at the attach file step.
Mass Spectrometry Imaging Raw Data Files (Original data) (Zenodo).

Acknowledgements

We thank the British Heart Foundation (RE/08/001), Dr Diran Elizabeth Kay Research Award and Translational Medicine Research Collaboration (Wyeth) for funding. TG received support from the STARSS project (Reg. No. CZ.02.1.01/0.0/0.0/15_003/0000465) co-funded by ERDF, and the Project of Specific Research SVV 260 662. For the purpose of open access, the authors have applied a Creative Commons Attribution (CC BY) license to any Author Accepted Manuscript version arising from this submission. Experiments were conducted at the Edinburgh Clinical Research MS Core (RRID:SCR_021833) and the Scottish Instrumentation and Research Centre for Advanced MS.

Appendix A. Supplementary data

Supplementary data to this article can be found online at https://doi.org/10.1016/j.talanta.2024.126954.

References

[1] R. Amit, D. Sanchit, U. Muhammad, L. Miranda, K. Dinesh, Atherosclerotic cardiovascular disease risk prediction: current state-of-the-art, Heart (2023), https://doi.org/10.1136/heartjnl-2023-322928 heartjnl-2023-322928.
[2] V. Fuster, P.R. Moreno, Z.A. Fayad, R. Corti, J.J. Badimon, Atherothrombosis and high-risk plaque: Part I: evolving concepts, J. Am. Coll. Cardiol. 46 (6) (2005) 937–954, https://doi.org/10.1016/j.jacc.2005.03.074.
[3] P.A. Mundra, C.K. Barlow, P.J. Nestel, E.H. Barnes, A. Kirby, P. Thompson, D. R. Sullivan, Z.H. Alshehry, N.A. Mellett, K. Huynh, K.S. Jayawardana, C. Giles, M. J. McConville, S. Zoungas, G.S. Hillis, J. Chalmers, M. Woodward, G. Wong, B. A. Kingwell, J. Simes, A.M. Tonkin, P.J. Meikle, Large-scale plasma lipidomic profiling identifies lipids that predict cardiovascular events in secondary prevention, JCI insight 3 (17) (2018), https://doi.org/10.1172/jci.insight.121326.
[4] C. Stegemann, R. Pechlaner, P. Willeit, S.R. Langley, M. Mangino, U. Mayr, C. Menni, A. Moayyeri, P. Santer, G. Rungger, T.D. Spector, J. Willeit, S. Kiechl, M. Mayr, Lipidomics profiling and risk of cardiovascular disease in the prospective population-based bruneck study, Circulation 129 (18) (2014) 1821–1831, https://doi.org/10.1161/CIRCULATIONAHA.113.002500.
[5] C. Weber, H. Noels, Atherosclerosis: current pathogenesis and therapeutic options, Nat. Med. 17 (11) (2011) 1410–1422, https://doi.org/10.1038/nm.2538.
[6] F. Hoffmann, C. Umbreit, T. Krüger, D. Pelzel, G. Ernst, O. Kniemeyer, O. Guntinas-Lichius, A. Berndt, F. von Eggeling, Identification of proteomic markers in head and neck cancer using MALDI–MS imaging, LC–MS/MS, and, Immunohistochemistry, Proteom. - Clin. Appl. 13 (1) (2019) 1700173, https://doi.org/10.1002/prca.201700173.
[7] K. Nakagawa, M. Tanaka, T.-H. Hahm, H.-N. Nguyen, T. Matsui, Y.-X. Chen, Y. Nakashima, Accumulation of plasma-derived lipids in the lipid core and necrotic core of human atheroma: imaging mass spectrometry and histopathological analyses, Arterioscler. Thromb. Vasc. Biol. 41 (11) (2021) e498–e511, https://doi.org/10.1161/ATVBAHA.121.316154.
[8] E.H. Seeley, Z. Liu, S. Yuan, C. Stroope, E. Cockerham, N.A. Rashdan, L. F. Delgadillo, A.C. Finney, D. Kumar, S. Das, B. Razani, W. Liu, J. Traylor, A.W. Orr, O. Rom, C.B. Pattillo, A. Yurdagul, Spatially resolved metabolites in stable and unstable human atherosclerotic plaques identified by mass spectrometry imaging, Arterioscler. Thromb. Vasc. Biol. 43 (9) (2023) 1626–1635, https://doi.org/10.1161/ATVBAHA.122.318684.
[9] A.M. Moerman, M. Visscher, N. Slijkhuis, K. Van Gaalen, B. Heijs, T. Klein, P. C. Burgers, Y.B. De Rijke, H.M.M. Van Beusekom, T.M. Luider, H.J.M. Verhagen, A. F.W. Van der Steen, F.J.H. Gijsen, K. Van der Heiden, G. Van Soest, Lipid signature of advanced human carotid atherosclerosis assessed by mass spectrometry imaging, J. Lipid Res. 62 (2021) 100020, https://doi.org/10.1194/jlr.RA120000974.
[10] J. Fan, M. Niimi, Y. Chen, R. Suzuki, E. Liu, Use of rabbit models to study AtherosclerosisAtherosclerosis, in: D. Ramji (Ed.), Atherosclerosis: Methods and Protocols, Springer US, New York, NY, 2022, pp. 413–431.
[11] R. Corti, J. Osende, R. Hutter, J.F. Viles-Gonzalez, U. Zafar, C. Valdivieso, G. Mizsei, J.T. Fallon, V. Fuster, J.J. Badimon, Fenofibrate induces plaque regression in hypercholesterolemic atherosclerotic rabbits: in vivo demonstration by high-resolution MRI, Atherosclerosis 190 (1) (2007) 106–113, https://doi.org/10.1016/j.atherosclerosis.2006.02.036.
[12] G. Pundziute, J.D. Schuijf, J.W. Jukema, I. Decramer, G. Sarno, P.K. Vanhoenacker, E. Boersma, J.H.C. Reiber, M.J. Schalij, W. Wijns, J.J. Bax, Evaluation of plaque characteristics in acute coronary syndromes: non-invasive assessment with multi-slice computed tomography and invasive evaluation with intravascular ultrasound

radiofrequency data analysis, Eur. Heart J. 29 (19) (2008) 2373–2381, https://doi.org/10.1093/eurheartj/ehn356.
[13] M. Jain, A. Frobert, J. Valentin, S. Cook, M.N. Giraud, The rabbit model of accelerated atherosclerosis: a methodological perspective of the iliac artery balloon injury, J. Vis. Exp. 128 (2017), https://doi.org/10.3791/55295.
[14] A. Dannhorn, E. Kazanc, S. Ling, C. Nikula, E. Karali, M.P. Serra, J.-L. Vorng, P. Inglese, G. Maglennon, G. Hamm, J. Swales, N. Strittmatter, S.T. Barry, O. J. Sansom, G. Poulogiannis, J. Bunch, R.J.A. Goodwin, Z. Takats, Universal sample preparation unlocking multimodal molecular tissue imaging, Anal. Chem. 92 (16) (2020) 11080–11088, https://doi.org/10.1021/acs.analchem.0c00826.
[15] A. Mehlem, C.E. Hagberg, L. Muhl, U. Eriksson, A. Falkevall, Imaging of neutral lipids by oil red O for analyzing the metabolic status in health and disease, Nat. Protoc. 8 (6) (2013) 1149–1154, https://doi.org/10.1038/nprot.2013.055.
[16] L. Goracci, S. Tortorella, P. Tiberi, R.M. Pellegrino, A. Di Veroli, A. Valeri, G. Cruciani, Lipostar, a comprehensive platform-neutral cheminformatics tool for lipidomics, Anal. Chem. 89 (11) (2017) 6257–6264, https://doi.org/10.1021/acs.analchem.7b01259.
[17] G. Liebisch, E. Fahy, J. Aoki, E.A. Dennis, T. Durand, C.S. Ejsing, M. Fedorova, I. Feussner, W.J. Griffiths, H. Köfeler, A.H. Merrill Jr., R.C. Murphy, V. B. O'Donnell, O. Oskolkova, S. Subramaniam, M.J.O. Wakelam, F. Spener, Update on LIPID MAPS classification, nomenclature, and shorthand notation for MS-derived lipid structures, J. Lipid Res. 61 (12) (2020) 1539–1555, https://doi.org/10.1194/jlr.S120001025.
[18] H. Sun, J. Zhao, D. Zhong, G. Li, Potential serum biomarkers and metabonomic profiling of serum in ischemic stroke patients using UPLC/Q-TOF MS/MS, PLoS One 12 (12) (2017) e0189009, https://doi.org/10.1371/journal.pone.0189009.
[19] B. Galindo-Prieto, L. Eriksson, J. Trygg, Variable influence on projection (VIP) for orthogonal projections to latent structures (OPLS), J. Chemom. 28 (8) (2014) 623–632, https://doi.org/10.1002/cem.2627.
[20] X. Han, R.W. Gross, Structural determination of lysophospholipid regioisomers by electrospray ionization tandem mass spectrometry, J. Am. Chem. Soc. 118 (2) (1996) 451–457, https://doi.org/10.1021/ja952326r.
[21] X. Liu, J. Gao, J. Chen, Z. Wang, Q. Shi, H. Man, S. Guo, Y. Wang, Z. Li, W. Wang, Identification of metabolic biomarkers in patients with type 2 diabetic coronary heart diseases based on metabolomic approach, Sci. Rep. 6 (1) (2016) 30785, https://doi.org/10.1038/srep30785.
[22] W. Li, J. Luo, F. Peng, R. Liu, X. Bai, T. Wang, X. Zhang, J. Zhu, X.-Y. Li, Z. Wang, W. Liu, J. Wang, L. Zhang, X. Chen, T. Xue, C. Ding, C. Wang, L. Jiao, Spatial metabolomics identifies lipid profiles of human carotid atherosclerosis, Atherosclerosis 364 (2023) 20–28, https://doi.org/10.1016/j.atherosclerosis.2022.11.019.
[23] C. Zhang, K. Wang, L. Yang, R. Liu, Y. Chu, X. Qin, P. Yang, H. Yu, Lipid metabolism in inflammation-related diseases, Analyst 143 (19) (2018) 4526–4536, https://doi.org/10.1039/C8AN01046C.
[24] A. Schober, W. Siess, Lysophosphatidic acid in atherosclerotic diseases, Br. J. Pharmacol. 167 (3) (2012) 465–482, https://doi.org/10.1111/j.1476-5381.2012.02021.x.
[25] N. Shah, R. Sethi, S. Shah, K. Jafri, J. Duran, Y. Chang, C. Soni, H. Wollocko, The roles of platelet-activating factor and magnesium in pathophysiology of hypertension, atherogenesis, cardiovascular disease, stroke and aging, Cardiogenetics 12 (1) (2022) 49–62, https://doi.org/10.3390/cardiogenetics12010005.
[26] M. Piccoli, F. Cirillo, A. Ghiroldi, P. Rota, S. Coviello, A. Tarantino, P. La Rocca, I. Lavota, P. Creo, P. Signorelli, C. Pappone, L. Anastasia, Sphingolipids and atherosclerosis: the dual role of ceramide and sphingosine-1-phosphate, Antioxidants (2023), https://doi.org/10.3390/antiox12010143.
[27] F. Cirillo, M. Piccoli, A. Ghiroldi, M.M. Monasky, P. Rota, P. La Rocca, A. Tarantino, S. D'Imperio, P. Signorelli, C. Pappone, L. Anastasia, The antithetic role of ceramide and sphingosine-1-phosphate in cardiac dysfunction, J. Cell. Physiol. 236 (7) (2021) 4857–4873, https://doi.org/10.1002/jcp.30235.
[28] S. Borodzicz, K. Czarzasta, M. Kuch, A. Cudnoch-Jedrzejewska, Sphingolipids in cardiovascular diseases and metabolic disorders, Lipids Health Dis. 14 (1) (2015) 55, https://doi.org/10.1186/s12944-015-0053-y.
[29] S. Marathe, S.L. Schissel, M.J. Yellin, N. Beatini, R. Mintzer, K.J. Williams, I. Tabas, Human vascular endothelial cells are a rich and regulatable source of secretory sphingomyelinase: implications for early atherogenesis and ceramide-mediated cell signaling, J. Biol. Chem. 273 (7) (1998) 4081–4088, https://doi.org/10.1074/jbc.273.7.4081.
[30] I. Tabas, Nonoxidative modifications of lipoproteins in atherogenesis, Annu. Rev. Nutr. 19 (1) (1999) 123–139, https://doi.org/10.1146/annurev.nutr.19.1.123.
[31] M. Taniguchi, T. Okazaki, Ceramide/sphingomyelin rheostat regulated by sphingomyelin synthases and chronic diseases in murine models, J Lipid Atheroscler 9 (3) (2020) 380–405, https://doi.org/10.12997/jla.2020.9.3.380.
[32] R. Virmani, F.D. Kolodgie, A.P. Burke, A. Farb, S.M. Schwartz, Lessons from sudden coronary death, Arterioscler. Thromb. Vasc. Biol. 20 (5) (2000) 1262–1275, https://doi.org/10.1161/01.ATV.20.5.1262.
[33] F.D. Kolodgie, K. Yahagi, H. Mori, M.E. Romero, H.H. Trout, A.V. Finn, R. Virmani, High-risk carotid plaque: lessons learned from histopathology, Semin. Vasc, Surg. 30 (1) (2017) 31–43, https://doi.org/10.1053/j.semvascsurg.2017.04.008.
[34] J.L. Harman, H.F. Jørgensen, The role of smooth muscle cells in plaque stability: therapeutic targeting potential, Br. J. Pharmacol. 176 (19) (2019) 3741–3753, https://doi.org/10.1111/bph.14779.
[35] T. Gerhardt, A. Haghikia, P. Stapmanns, D.M. Leistner, Immune mechanisms of plaque instability, Front. Cardiovasc. Med. 8 (2022), https://doi.org/10.3389/fcvm.2021.797046.
[36] N.E. Manicke, M. Nefliu, C. Wu, J.W. Woods, V. Reiser, R.C. Hendrickson, R. G. Cooks, Imaging of lipids in atheroma by desorption electrospray ionization mass spectrometry, Anal. Chem. 81 (21) (2009) 8702–8707, https://doi.org/10.1021/ac901739s.
[37] S.B. Chatterjee, S. Dey, W.Y. Shi, K. Thomas, G.M. Hutchins, Accumulation of glycosphingolipids in human atherosclerotic plaque and unaffected aorta tissues, Glycobiology 7 (1) (1997) 57–65, https://doi.org/10.1093/glycob/7.1.57.
[38] T.D. Mullen, S. Spassieva, R.W. Jenkins, K. Kitatani, J. Bielawski, Y.A. Hannun, L. M. Obeid, Selective knockdown of ceramide synthases reveals complex interregulation of sphingolipid metabolism [S], J. Lipid Res. 52 (1) (2011) 68–77, https://doi.org/10.1194/jlr.M009142.
[39] A. Edsfeldt, P. Dunér, M. Ståhlman, I.G. Mollet, G. Asciutto, H. Grufman, M. Nitulescu, A.F. Persson, R.M. Fisher, O. Melander, M. Orho-Melander, J. Borén, J. Nilsson, I. Gonçalves, Sphingolipids contribute to human atherosclerotic plaque inflammation, Arterioscler. Thromb. Vasc. Biol. 36 (6) (2016) 1132–1140, https://doi.org/10.1161/ATVBAHA.116.305675.
[40] V.T. Dang, L.H. Zhong, A. Huang, A. Deng, G.H. Werstuck, Glycosphingolipids promote pro-atherogenic pathways in the pathogenesis of hyperglycemia-induced accelerated atherosclerosis, Metabolomics 14 (7) (2018) 92, https://doi.org/10.1007/s11306-018-1392-2.
[41] F. Bietrix, E. Lombardo, C.P. van Roomen, R. Ottenhoff, M. Vos, P.C. Rensen, A. J. Verhoeven, J.M. Aerts, A.K. Groen, Inhibition of glycosphingolipid synthesis induces a profound reduction of plasma cholesterol and inhibits atherosclerosis development in APOE* 3 Leiden and low-density lipoprotein receptor−/− mice, Arterioscler. Thromb. Vasc. Biol. 30 (5) (2010) 931–937, https://doi.org/10.1161/ATVBAHA.109.201673.
[42] T.O. Eichmann, A. Lass, DAG tales: the multiple faces of diacylglycerol—stereochemistry, metabolism, and signaling, Cell. Mol. Life Sci. 72 (20) (2015) 3931–3952, https://doi.org/10.1007/s00018-015-1982-3.
[43] D. Corda, P. Zizza, A. Varone, B.M. Filippi, S. Mariggiò, The glycerophosphoinositols: cellular metabolism and biological functions, Cell. Mol. Life Sci. 66 (21) (2009) 3449–3467, https://doi.org/10.1007/s00018-009-0113-4.
[44] R.W. Mahley, T.L. Innerarity, M.S. Brown, Y.K. Ho, J.L. Goldstein, Cholesteryl ester synthesis in macrophages: stimulation by beta-very low density lipoproteins from cholesterol-fed animals of several species, J. Lipid Res. 21 (8) (1980) 970–980, https://doi.org/10.1016/S0022-2275(20)34757-X.
[45] M.I. Cybulsky, M.A. Gimbrone, Endothelial expression of a mononuclear leukocyte adhesion molecule during atherogenesis, Science 251 (4995) (1991) 788–791, https://doi.org/10.1126/science.1990440.
[46] J. Fan, S. Kitajima, T. Watanabe, J. Xu, J. Zhang, E. Liu, Y.E. Chen, Rabbit models for the study of human atherosclerosis: from pathophysiological mechanisms to translational medicine, Pharmacol. Ther. 146 (2015) 104–119, https://doi.org/10.1016/j.pharmthera.2014.09.009.
[47] M.V. McConnell, M. Aikawa, S.E. Maier, P. Ganz, P. Libby, R.T. Lee, MRI of rabbit atherosclerosis in response to dietary cholesterol lowering, Arterioscler. Thromb. Vasc. Biol. 19 (8) (1999) 1956–1959, https://doi.org/10.1161/01.ATV.19.8.1956.
[48] M. Martin-Lorenzo, B. Balluff, A.S. Maroto, R.J. Carreira, R.J.M. van Zeijl, L. Gonzalez-Calero, F. de la Cuesta, M.G. Barderas, L.F. Lopez-Almodovar, L. R. Padial, L.A. McDonnell, F. Vivanco, G. Alvarez-Llamas, Molecular anatomy of ascending aorta in atherosclerosis by MS Imaging: specific lipid and protein patterns reflect pathology, J. Proteom. 126 (2015) 245–251, https://doi.org/10.1016/j.jprot.2015.06.005.
[49] C. Calcagno, O. Lairez, J. Hawkins, W. Kerr Steven, S. Dugas Melanie, T. Simpson, J. Epskamp, M. Robson Philip, M. Eldib, I. Bander, K.R. Purushothaman, S. Ramachandran, A. Pruzan, A. Kaufman, V. Mani, A. Ehlgen, G. Niessen Heiko, J. Broadwater, A. Fayad Zahi, Combined PET/DCE-MRI in a rabbit model of atherosclerosis, JACC (J. Am. Coll. Cardiol.): Cardiovasc. Imaging 11 (2_Part_2) (2018) 291–301, https://doi.org/10.1016/j.jcmg.2017.11.030.
[50] S. Ben-Aicha, L. Casaní, N. Muñoz-García, O. Joan-Babot, E. Peña, M. Aržanauskaitė, M. Gutierrez, G. Mendieta, T. Padró, L. Badimon, G. Vilahur, HDL (High-Density lipoprotein) remodeling and magnetic resonance imaging–assessed atherosclerotic plaque burden, Arterioscler. Thromb. Vasc. Biol. 40 (10) (2020) 2481–2493, https://doi.org/10.1161/ATVBAHA.120.314956.
[51] A. Daugherty, A.R. Tall, M.J.A.P. Daemen, E. Falk, E.A. Fisher, G. García-Cardeña, A.J. Lusis, A.P. Owens, M.E. Rosenfeld, R. Virmani, Recommendation on Design, execution, and reporting of animal atherosclerosis studies: a scientific statement from the American heart association, Arterioscler. Thromb. Vasc. Biol. 37 (9) (2017) e131–e157, https://doi.org/10.1161/ATV.0000000000000062.
[52] F. Eichelmann, L. Sellem, C. Wittenbecher, S. Jäger, O. Kuxhaus, M. Prada, R. Cuadrat, K.G. Jackson, J.A. Lovegrove, M.B. Schulze, Deep lipidomics in human plasma: cardiometabolic disease risk and effect of dietary fat modulation, Circulation 146 (1) (2022) 21–35, https://doi.org/10.1161/CIRCULATIONAHA.121.056805.
[53] G. Van Meer, D.R. Voelker, G.W. Feigenson, Membrane lipids: where they are and how they behave, Nat. Rev. Mol. Cell Biol. 9 (2) (2008) 112–124, https://doi.org/10.1038/nrm2330.
[54] O.G. Abela, C.H. Ahsan, F. Alreefi, N. Salehi, I. Baig, A. Janoudi, G.S. Abela, Plaque rupture and thrombosis: the value of the atherosclerotic rabbit model in defining the mechanism, Curr. Atheroscler. Rep. 18 (6) (2016) 29, https://doi.org/10.1007/s11883-016-0587-0.